Granular shear flow dynamics and forces: Experiment and continuum theory

L. Bocquet,[1,2] W. Losert,[3,*] D. Schalk,[3] T. C. Lubensky,[2] and J. P. Gollub[2,3]
[1]*Laboratoire de Physique de l'ENS de Lyon, UMR CNRS 5672, 46 Allée d'Italie, 69364 Lyon Cedex, France*
[2]*Physics Department, University of Pennsylvania, Philadelphia, Pennsylvania 19104*
[3]*Physics Department, Haverford College, Haverford, Pennsylvania 19041*
(Received 19 December 2000; published 21 December 2001)

We analyze the main features of granular shear flow through experimental measurements in a Couette geometry and a comparison to a locally Newtonian, continuum model of granular flow. The model is based on earlier hydrodynamic models, adjusted to take into account the experimentally observed coupling between fluctuations in particle motion and mean-flow properties. Experimentally, the local velocity fluctuations are found to decrease more slowly with distance from the shear surface than the velocity. This can be explained by an effective viscosity that diverges more rapidly as the random-close-packing density is approached than is predicted by Enskog theory for dense hard-sphere systems. Experiment and theory are in good agreement, especially for the following key features of granular flow: The flow is confined to a small shear band, fluctuations decay approximately exponentially away from the sheared wall, and the shear stress is approximately independent of the shear velocity. The functional forms of the velocity and fluctuation profiles predicted by the model agree with the experimental results.

DOI: 10.1103/PhysRevE.65.011307 PACS number(s): 45.70.Mg, 83.50.Ax, 47.50.+d

I. INTRODUCTION

The general features of granular shear flow have been investigated thoroughly over the last several years [1,2]. The following key points emerge in shear flow experiments on a large range of materials in two and three dimensions:

The velocity of particles decreases quickly over a few particle diameters away from the shearing wall (see, e.g., [2–4]).

(i) The velocity profile, normalized by the shear velocity U, is independent of U (see, e.g., [2,3]).

(ii) The shear force σ is approximately independent of U, if the granular material is allowed to dilate (see, e.g., [8]).

(iii) These features, together with the discovery of strong inhomogeneities in the force distribution even during flow [2,9], might be taken to indicate that any continuum approach, such as local hydrodynamic models, should fail to describe granular flow.

Here, we revisit the assumptions made in earlier hydrodynamic models of granular flow, via careful comparison to the experimentally measured microscopic particle dynamics in a circular Couette geometry. This leads us to emphasize the strong interplay between local rms fluctuations, the mean flow, and the local density. When this coupling is properly taken into account, a hydrodynamic model, which we have introduced in Ref. [10], quantitatively describes all key properties of granular shear flow discussed above, including both flow properties and shear forces.

The shear force obtained from the hydrodynamic model resembles the simple dynamic friction law found in solid-on-solid friction, i.e., the shear force is proportional to pressure, but approximately independent of shear velocity. We emphasize that this result is obtained even though the hydrodynamic model does not include frictional forces between grains.

The temperature is defined here as the mass times the square of rms-velocity fluctuations. While the temperature is a constant in shear flow of an ordinary fluid, granular temperature is dissipated through inelastic collisions. Its spatial variation plays a crucial role in determining the properties of granular flow. We find that the granular temperature profile, normalized by its maximum value, is roughly independent of shear velocity and pressure. Temperature is introduced into the system via viscous heating over a characteristic length of the order of a few particle diameters. It is then dissipated via inelastic collisions over a longer length scale. Our model contains a description of the source and transport of fluctuations that allows us to predict the pressure and the shear velocity dependence of both the shear forces and the particle dynamics.

In the experiments reported here, which go beyond those reported earlier [10], the granular material is sheared in a Couette geometry with a rotating inner cylinder and a stationary outer cylinder. The inner cylinder is connected to the motor through a flexible spring that allows either stick-slip motion or steady shearing depending on parameters. We may also apply an upward air flow at a variable rate through the granular material to dilate the material and reduce the stresses. Our ability to vary the stresses via air flow, and our study of both stick-slip and steady dynamics in the same apparatus, distinguish this paper from other experimental measurements of sheared granular matter [3,2].

In addition to performing force measurements, which probe macroscopic material properties of the ensemble of particles, we determine the dynamics of individual particles by measuring the mean-velocity and rms-velocity fluctuations of particles on the top surface of the granular layer. The combination of velocity and force measurements, together with variation of the stresses and the time dependence of the flow, allow for a very sensitive test of our theoretical model.

*Present address: Dept. of Physics and IPST, Univ. of Maryland, College Park, Maryland 20742.

Previous experimental results and modeling approaches are reviewed in Sec. II. Our experimental setup and results for the particle dynamics and shear forces in sheared granular matter are discussed in Secs. III and IV. In Sec. V, the locally Newtonian hydrodynamic model is described in detail. We conclude in Sec. VI with a discussion of the main results and the broader implications of this paper.

II. BACKGROUND

Efforts to understand particle dynamics during granular flow may be roughly divided into adaptations of continuum models, based on hydrodynamic or elastoplastic descriptions, and models that emphasize the differences between molecular fluids or solids and granular matter, such as the inhomogeneous character of particle contacts and of stress transmission in a granular material. In this section, we review briefly these different approaches. We conclude with a discussion of the aim of our hydrodynamic model in the context of previous work.

A. Continuum models of granular flow

Hydrodynamic models were motivated by Bagnolds pioneering theoretical and experimental work on shear forces in dense suspensions [11]. The constitutive equations for macroscopic quantities, such as the shear stress as a function of shear rate, were investigated in several studies of dense suspensions with fixed volume. In the limit of large velocities, Bagnold found that in a fixed volume, the shear stress σ is proportional to the shear velocity U squared. He referred to this regime as the ''grain inertia regime.'' He accounted for the measurements by assuming that the local shear stress σ was proportional to the square of the local shear rate $\dot{\gamma}$. He justified such a relationship on the basis of kinetic arguments. Since direct measurements of microscopic particle dynamics were not available, he assumed a linear velocity profile similar to that of ordinary fluids.

The development of hydrodynamic descriptions, extracted from the ''microscopic'' dynamics using kinetic theory, was pioneered by Jenkins and Savage [12] and by Haft [13]. A considerable amount of theoretical, numerical, and experimental work has refined and modified this approach. Reviews of models of granular flow that describe many of these studies has been compiled by Campbell [14], Savage [15], and more recently, by Clement [1].

In the kinetic theory approach, the granular material is generally modeled as an inelastic hard-sphere system. Constitutive equations similar to the usual Navier-Stokes equations of hydrodynamics may be obtained in the limit of small inelasticity. The transport coefficients entering the flow equations are usually computed at the level of the Enskog equation [38], an extension of the Boltzmann equation that takes the finite size of particles into account but neglects correlations between collisions. Due to the assumptions that enter into the kinetic theories presented above, these descriptions are limited to rapid granular flows and to intermediate or low-particle densities.

In order to understand the boundary between a seemingly flowing state and an apparently stationary state, various extensions of the previous hydrodynamic model have been proposed. Jenkins and Askari [16] have studied the interface between a flowing region and an amorphous (high-density) region that is at rest. In this paper, the thickness of the shear band is determined by the balance between the energy input and the loss rate due to inelasticity. On the other hand, viscoplastic models have been proposed. The Savage-Hutter model [17] uses the Mohr-Coulomb failure criterion to predict the transition from solidlike to fluidlike behavior in the context of avalanching and rock slides. The constitutive relation connecting shear stress to shear rate is of great practical importance. Different relations have been proposed for various situations, and several are summarized in a table in [18].

B. Alternative descriptions of granular flow

Beyond measurements of the mean properties (such as shear forces) that are important for a continuum model, recent experimental and theoretical studies have focused on measurements of the particle dynamics and shear forces at the scale of an individual particle.

Detailed measurements of the particle dynamics (see, e.g., [2–4]) revealed that in several experimental geometries particle motion is confined to several (generally 5–10) particle diameters close to the sheared surface. The velocity profile is found to be roughly exponential or Gaussian.

Velocity fluctuations have been determined in dense granular flows in different flow geometries. Space-averaged velocity fluctuations were measured with high-temporal resolution in the interior of a granular chute flow using diffusing-wave spectroscopy [5]. Fluctuations at the level of individual particle motion were determined using video imaging of tracer particles [6], though the video frame rate may not be sufficient to capture all fluctuations between collisions [5]. High-speed digital video imaging was used to determine velocity fluctuations in a vertically vibrated granular material [7].

The force distribution within a granular assembly, measured with birefringent disks [19] or carbon paper [20], was found to exhibit strong inhomogeneities on the particle scale. Stresses were found to be transmitted along chains of particles (force chains) in a static granular assembly and during shear.

There have been several attempts to account specifically for these inhomogeneities in granular flows. Some approaches describe the flow properties on the basis of fracture models [21,22], while others introduced nonlocal constitutive equations coupling force chains to flowing grains [23].

The shear strength of deformable, inelastic spheres was modeled using a discrete element method by Aharonov and Sparks [9]. The density is found to adjust to a critical density within the shear band.

C. Our hydrodynamic model

While theories and models of granular flow have become remarkably detailed, the assumptions of each model may

strongly influence the results. As noted by Campbell [14], detailed experimental measurements of particle velocities, granular temperatures, and densities were often unavailable when models were developed. The measurements reported here should help assess the validity of the assumptions of various models.

Here, we revisit the local hydrodynamic model and carefully reexamine the assumptions made to derive the constitutive equations in view of our experimental measurements of individual particle dynamics and mean shear forces.

The mean shear forces have been studied before in an experimental system similar to ours: Tardos *et al.* [8] investigated the effect of an upward air flow through the granular material on the shear forces. The shear force was found to decrease linearly with air flow. On the basis of Bagnold's results [11] and much subsequent work, it is clear that dilatancy has an important effect on granular flow. This was also convincingly demonstrated in the experiments by Tardos *et al.*: If the material is allowed to expand, the shear stress is independent of shear velocity. On the other hand, if the material is confined to a fixed volume, Bagnold's result of a quadratic increase of shear stress with shear velocity is found.

The interplay between dilatancy, fluctuations, and flow is complex. Theoretical investigations have not yet produced results that are consistent with measured mean (macroscopic) properties and measured dynamics at the particle (microscopic) scale. Granular material develops a greater resistance to flow as its density increases. Previous theoretical treatments of granular flow have either been restricted to the lower-density rapid-flow regime [1], or they have incorporated a yield threshold (viscoplastic models) that produces a well-defined transition from liquidlike to solidlike behavior [17].

Recent experimental studies of granular flow down a sandpile by Komatsu *et al.* [24] using a long exposure-time video imaging have revealed that the transition between solidlike and fluidlike behavior may not be very well defined. The velocity profile within the flowing layer was found to be exponential over more than seven orders of magnitude in speed with no clear transition to a solidlike state. These results indicate that no strict transition may exist, but instead, one may be able to treat the solidlike state as a very high-viscosity fluid.

As emphasized in the literature review given in Sec. II A and II B, two alternate directions may conceivably be followed in order to describe granular shear flows in the high-density, finite-velocity regime. One might try to extend quasistatic descriptions based on friction and elasticity to the finite-velocity case. Alternately, one may start from a hydrodynamic model, which is appropriate *a priori* in the high-velocity collisional regime, and modify it to ensure that high-density effects are properly taken into account. In the present paper, we have chosen the second route, and we show that the inclusion of such high-density effects allows for a coherent description of various experimental results for shear flows. Although the model does not include solid friction between the grains, friction forces will in fact become important in the quasistatic limit, where contacts endure and the model is expected to fail.

Previous approaches [12,13] have used the Enskog kinetic theory to derive the hydrodynamic equations appropriate to describe granular material in the collisional regime. These approaches correctly take into account the excluded volume between colliding particles. However, since they are based on a Boltzmann-Stosszahlansatz assumption, they neglect any correlation between encounters. Such an assumption breaks down at large densities where correlated motion of particles occur, e.g., through cooperative rearrangements. In elastic systems (i.e., *those without energy loss during collisions*), the viscosity is then found to exhibit an anomalous divergence with density in the high-density limit [26–28]. The divergence with density is roughly equivalent to the divergence with decreasing temperature for a supercooled liquid close to the glass transition [29]. Such anomalous effects are expected to occur in granular material close to the random close packing (RCP), which is experimentally found to be 63.7% for slightly polydisperse systems [25]. For a wider distribution of particle sizes, larger densities can be reached.

In our paper, we explicitly include such high-density effects in the hydrodynamic equations. This leads to theoretical predictions in quantitative agreement with most of our experimental results. It also provides a direct connection between the dynamics of granular media and glasses, as has been proposed by Liu and Nagel [30].

III. EXPERIMENTAL SETUP

A. Apparatus

In the experiments, we shear the granular material in a Couette geometry. The granular material used in most of the experiments reported here consists of $0.55-0.95$ mm diameter black glass beads (from Jaygo Inc.) ($\rho_m = 2.55$ g/cm^3). The color does not alter surface properties, but increases the opacity of the material, which facilitates the tracking of particles on the surface as described below. We also carried out experiments with a mixture of 1.3 and 1.6 mm chrome steel spheres ($\rho_m = 5.0$ g/cm^3), and with polydisperse, rough ceramic spheres (Macrolite ML1430 from Kinetico Corp.) with diameter $0.83-1.47$ mm ($\rho_m = 0.51$ g/cm^3).

In the experimental apparatus, the granular material is confined to a 12 mm gap between a stationary outer cylinder and a rotating inner cylinder ($r = 51$ mm), as shown in Fig. 1. The gap can be reduced to 3 mm. The inner cylinder is hollow to reduce its inertia and is coated with a monolayer of randomly packed glass beads to provide a rough boundary. The outer glass cylinder is coated with a monolayer of randomly packed glass beads up to the height of the top surface, which allows observation of the top layer of grains through a mirror as shown in Fig. 1. The lower 38 mm of the inner cylinder is stationary in order to minimize boundary layer effects.

To shear the material, the inner cylinder is rotated with a 4000 step/turn microstepping motor (from Aerotech Inc.) at a variable rate of $0.001-1$ Hz. The rotation rate is smoothed by a 100:1 gearhead for rates <1 Hz. The rotation rate ω of the cylinder imposes the shear velocity U at the boundary of

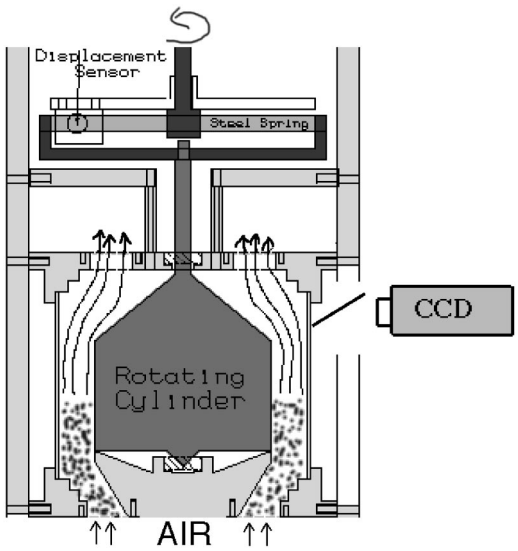

FIG. 1. Experimental setup: The granular material (between two concentric cylinders) is fluidized by an upward air flow and sheared by rotation of the inner cylinder, which is connected to the motor through a flexible spring. Shear forces are determined from the spring displacement. Particle motions in the top layer are measured through the glass outer cylinder with a fast CCD camera.

the granular material as through $U=2\pi r\omega$, with $r=51$ mm the radius of the inner cylinder. The inner cylinder is connected to the microstepping motor via a flexible tempered steel spring. This spring configuration allows us to measure instantaneous shear forces with excellent dynamic range and precision, since the spring bending is proportional to the applied shear force. We measure the spring bending with a capacitive displacement sensor (EMD1051, Electro Corp.) that is rigidly connected to the motor shaft at a radial distance of 4.2 mm from the shaft. The spring constant of the spring (dimensions: $0.51\times7.5\times165$ mm) was determined to be 220 ± 8 N/m.

The soft connection between the motor and the inner cylinder permits both stick-slip dynamics and continuous motion of the inner cylinder to be obtained, depending on parameters. However, when a uniform speed of the cylinder is required for the experiment, the spring is replaced with a rigid connection. In that case, measurement of shear forces is not possible.

We may also apply an upward air flow at a variable rate through the granular material. The air flow enters the granular material through a circular opening between the cylinders, and leaves the granular material through a circularly symmetric opening at the top. This assures a uniform airflow rate throughout the material. Flow-rate uniformity was tested by observing the position of air bubbles as they leave the upper surface of the granular material. Air bubbles form at high-flow rates in the class of granular materials used in this experiment. The random position of air bubbles indicates that the flow is uniformly distributed throughout the gap. Except for this test for flow uniformity, none of the experiments presented in this paper was carried in the presence of air bubbling. The air flow is provided by a blower (Rigid Inc.) operated at variable input ac voltage. Flow rates are measured by means of an air velocity transducer (FMA 904, Omega Inc.). For the range of air-flow rates we employed, the average density of the granular material changes by less than 10% and the flow speed is calculated in first approximation assuming the porosity for random close packing.

Since the air flow exerts a drag on individual grains, the effective weight supported by neighboring grains decreases with increasing upward airflow. This effective weight of individual grains, in turn, should be proportional to the pressure inside the granular material. We may, therefore, reduce the pressure by applying an upward air flow, and increase pressure by applying a downward air flow. The proportionality factor between air flow and pressure can be roughly estimated by calculating the upward drag exerted on a single sphere at the mean-air-flow speed within the granular material [31].

B. Determination of particle dynamics

We measure the mean particle velocities $V(y)$ and the velocity fluctuations $\delta V(y)$ on the upper surface of the granular material. These should approximate particle motion in the interior based on previous measurements [3] that found very similar velocity profiles in the interior (measured with magnetic resonance imaging (MRI) and x-ray techniques) and on the bottom surface of a shear cell. We return to this issue in Sec. VI.

The trajectories of individual particles in the surface layer are determined with a fast charge-coupled device (CCD) camera at $30-1000$ frames/sec. Particle motion is extracted from four sequences of 2000 images using procedures written in interactive data language (IDL) (RSI Inc.) based on tracking routines provided by J. Crocker and E. Weeks.

In the first step of the tracking process, both long-range brightness fluctuations (i.e., nonuniform illumination) and short-wavelength noise are reduced by applying a bandpass filter with a short-wavelength noise cutoff and a long-wavelength cutoff of roughly one-particle diameter. In the second step, the positions of particles (roughly 100 in each image) are determined by calculating the centroid of each bright region in the filtered image. This yields a spatial resolution of <0.1 pixels, provided that the bright region is several particle diameters wide. Black glass beads are better suited than undyed glass beads for an accurate determination of particle positions, since black beads are more opaque. This reduces internal reflections and reflections from particles in deeper layers. In order to improve spatial resolution, the intensity peaks are broadened by taking images slightly out of focus. The broader intensity peaks improve the precision of the centroid determination. Defocusing also reduces the intensity of secondary peaks due to scattering by multiple particles to a level where they are no longer interpreted as particles. For the ceramic particles, the defocusing process eliminates multiple peaks due to the substructure of individual particles.

In the third step of the trajectory determination, the particles are labeled and the evolution of their position through an image sequence is determined. The assignment of par-

ticles to corresponding points in the previous and next frame is based on a tracking algorithm, which minimizes the total squared displacement within a sequence of frames. In a final step, the probability distribution of individual particle displacements is used to verify that large displacement particles are not systematically cut off.

Since the mean-flow velocity V is comparable to the rms-velocity fluctuations close to the inner cylinder, accurate tracking of particles is only possible if the maximum displacement is considerably smaller than the distance between particles. We have verified that particles are accurately tracked, even when the maximum particle displacement between frames approaches the particle spacing.

From the particle tracks we determine average particle velocities $V(y)$ and rms-velocity fluctuations perpendicular to the flow direction $[\delta V_x(y)]$ and parallel to it $[\delta V_y(y)]$ as a function of distance y from the rotating inner cylinder. The position resolution of <0.1 pixel yields a resolution of particle velocities and fluctuations of better than 0.1 pixel/frame. The upper limit for measurable velocities is given by the tracking routine, which requires that the maximum displacement be smaller than one-particle diameter. Larger particle images yield a larger velocity range, but the velocity profile may not improve since fewer particles may be tracked in a single image. A mean-particle size of about 20 pixels gives sufficient dynamic range for the velocities with good statistics.

The measurement of rms velocity fluctuations captures changes in velocities on the timescale of our measurement (of up to 1000 frames per second). Collisions on a faster timescale smooth out the measured fluctuations. Since average collision times near the sheared surface (estimated from average speeds and densities) are comparable to the framerate, we are close to capturing true velocity fluctuations. We note that the collision rate may increase with increasing density away from the inner cylinder. The true fluctuations may therefore decay even more slowly with distance from the inner cylinder than the measured fluctuations described below. Higher-frame-rate measurements of local fluctuations, with simultaneous higher-spatial resolution would be required to improve the fluctuation measurements.

IV. EXPERIMENTAL RESULTS

A. Particle Dynamics

The behavior of the inner cylinder is found to be very similar to the dynamics of a rough plate sliding across a granular layer [32]. At low-shear rates, the motion of the inner cylinder is intermittent with short, rapid slips, and long periods of sticking. At sufficiently high-shear rates or with a stiff connection between motor and cylinder, steady motion of the inner cylinder is observed. Air flow reduces the shear forces, as already noted by Tardos *et al.* [8], and it also suppresses stick-slip motion.

The velocity profile $V(y)$, when normalized by the shear velocity U, is roughly independent of U, as shown in Fig. 2. Note that, as we have mentioned previously, the shear velocity U is computed from the rotation rate of the cylinder ω through $U=2\pi r\omega$, with $r=51$ mm the radius of the inner cylinder. The mean-velocity profile without air flow in the stick-slip regime (solid triangles) is essentially the same as that for steady shearing. The dashed line shows the theoretical prediction from our hydrodynamic model, which will be discussed in Sec. V.

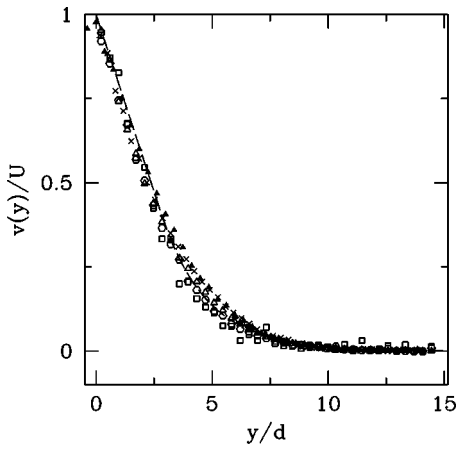

FIG. 2. Mean-particle velocity (normalized by the shear velocity) as a function of distance from the inner cylinder (in particle diameters) for glass spheres. The respective rotation rates of the inner cylinder are (in Hz) : 0.004 (hexagons), 0.04 (squares), 0.01 (open triangles), 0.4 (crosses). This corresponds to shear (with air flow) velocities U, respectively, equal (in mm/s) to 1.28, 12.8, 3.2, 128. The solid triangles show the velocity profile at a rotation rate of 0.01 Hz ($U=3.2$ mm/s) *without* air flow. The normalized mean-velocity profile is independent of shear velocity and shear dynamics (intermittent or steady motion). The dashed line is the solution of Eq. (28), with $\delta=4.7d$, $y_w=2.8d$, and $\alpha=0.4$ (see text for details).

Figure 3 shows the perpendicular rms-velocity fluctuations δV_y, which have not been previously measured in a

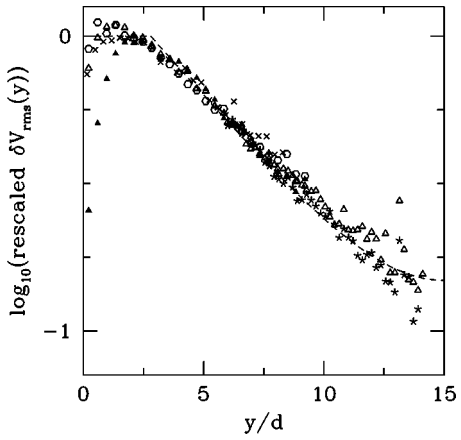

FIG. 3. rms-velocity fluctuations perpendicular to the shear direction. Fluctuations decrease roughly exponentially far from the inner cylinder, but more slowly than the mean flow. The rms fluctuations are rescaled (shifted vertically) such that all experimental points are forced to agree at $y=3d$, where d is the bead diameter. The dashed line is the theoretical result (see Sec. V), with a decay length $\delta=4.7d$ and a boundary position $y_w=2.8d$. Measurements are made on glass spheres, with symbols as in Fig. 2. The fluctuations could be underestimated, due to finite frame rate measurements, especially at larger y.

three-dimensional (3D) system to our knowledge. When data taken at different shear velocities U are normalized to the same magnitude at a distance of three-particle diameters away from the wall, the fluctuations follow the same profile, independent of shear velocity and independent of the presence or absence of stick-slip motion. The velocity fluctuations decrease roughly exponentially far from the inner cylinder but fall off more slowly with y than does the average velocity.

We determine fluctuations by averaging the velocity of a small section of the image over a long time and then calculating deviations of individual particle velocities from the mean of that section. The measured parallel fluctuation amplitude, therefore, includes fluctuations of the flow speed, which can be caused by the soft spring connection to the motor. In order to compare velocity fluctuations during stick-slip motion and steady shearing and to compare the measurements to the hydrodynamic model of a steady-state flow, we show only the perpendicular fluctuations. We note that even during steady shearing, parallel fluctuations are larger than perpendicular fluctuations, but their ratio remains roughly independent of y, as shown in Fig. 5 below.

In principle, the density profile could also be measured using the tracking algorithm, by counting the average number of tracked particles as a function of position y. In practice, however, no quantitative results could be obtained because of the limitation of the tracking method to resolve particle positions in the third dimension (e.g., for low densities, particles from lower layers are also counted: the density is thus quantitatively overestimated, while this does not affect the mean- and rms-velocity profiles). Qualitatively, the measured density profile increases with the radial coordinate toward a limiting value at large distances (not shown). The density close to the moving boundary is measured to be up to 40% below its limiting value, depending on shear velocity and airflow. The density increases rapidly with distance from the sheared surface over several particle diameters. This is in agreement with other numerical and experimental observations [3,37].

We now examine the particle behavior near the boundaries in more detail. Close to the inner cylinder, it is difficult to distinguish wall particles from particles that move close to the wall. Because we image the surface from a slight angle and because the height of particles fluctuates slightly, the boundary between wall particles and sheared particles fluctuates. We have examined the boundary conditions with both steel spheres and rough ceramic spheres, which allow us to distinguish the particles from the layer of rough glass beads glued to the inner cylinder. We find that the granular temperature has an approximately constant value in a region about three particle diameters wide near the inner wall (see Fig. 3).

Since particles barely move close to the stationary outer cylinder, the granular temperature at large y is examined at a lower frame rate than is necessary at positions close to the rapidly moving inner cylinder. This yields better statistics for the mean velocity, but leads to an underestimate of fluctuations in particle motion. Figure 4 shows the mean velocity and velocity fluctuations close to the outer wall. The velocity

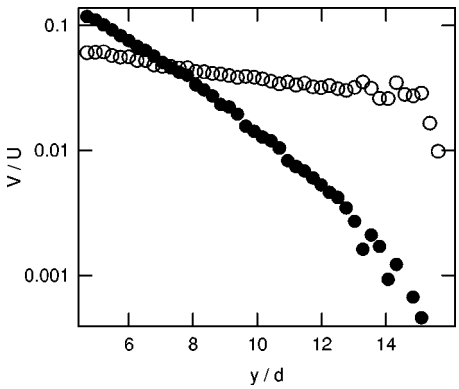

FIG. 4. Velocity (solid circles) and fluctuation profile (open circles) close to the stationary outer cylinder. Each profile is normalized by the shear velocity.

decreases roughly exponentially up to roughly two-particle diameters from the outer wall.

As discussed in the previous section, an upward airflow reduces the effective pressure, while a downward airflow increases the effective pressure within the material. This allows us to measure the pressure dependence of the velocity and fluctuation profile. Figure 5 shows three experiments at different air flow rates (i.e., pressure). In order to avoid stick-slip motion without airflow and with downward airflow, the motor is connected rigidly to the cylinder for these experiments. The crossing points of the temperature and velocity profiles in Figs. 4 and 5 are different because the mean velocity was different and the absolute value of the measured fluctuations depends on shear velocity.

Neither the velocity profile nor the profile of rms fluctuations (the granular temperature) change with pressure over the range of pressures accessible with this method. This is consistent with our hydrodynamic model as described in Sec. V. Note that the rms fluctuations parallel to the shear direction are larger by a factor of roughly 1.3, even though the

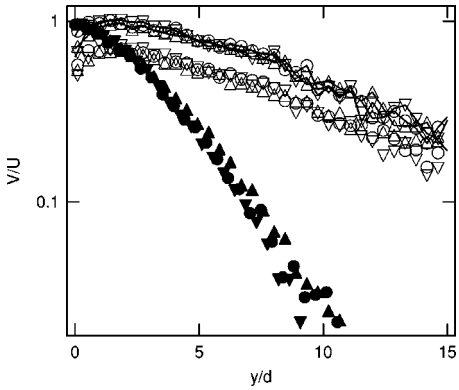

FIG. 5. Velocity profile $V(y)$ (solid symbols) and rms-fluctuation profile $\delta V(y)$ (open symbols) both perpendicular (no lines) and parallel (lines) to the shear direction at different effective pressures controlled by air flow. Measurements on glass spheres with upward airflow (triangles pointing up), no airflow (circles), and downward airflow (triangles pointing down). The measured fluctuation profiles do not depend significantly on the pressure, but do depend on the shear velocity.

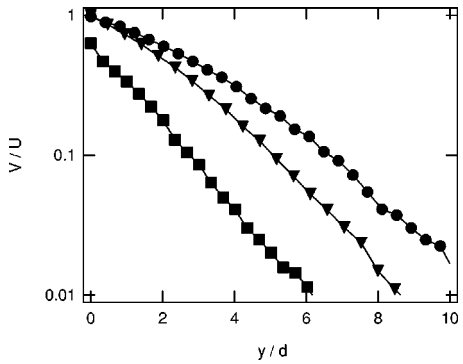

FIG. 6. Comparison of $V(y)$ for smooth glass spheres (circles), rough porous ceramic particles (triangles), and steel sphere mixtures (squares) at a rotation rate of 0.04 Hz, corresponding to $U = 12.8$ mm/s.

mean velocity cannot fluctuate due to the rigid connection between motor and cylinder. This anisotropy has been observed previously [33]. It may be connected to an anisotropy in pressure in a sheared granular system [34,35].

The velocity and fluctuation profiles are independent of shear velocity and shear dynamics, but may vary with the material that is sheared. The rms fluctuations decay significantly more slowly than the mean velocity for all materials. Our model contains three parameters that determine the velocity and fluctuation profiles, as discussed in Sec. V. These parameters may depend on material properties in a nontrivial way. In Fig. 6, we compare three very different materials (steel spheres, glass spheres, rough porous ceramic particles). For all materials, the mean velocity decays roughly exponentially far from the shear boundary. The characteristic length of that decay is between 1.5- and 2-particle diameters. The velocity of glass spheres decreases more slowly away from the sheared cylinder than does that of rough ceramic particles. Steel spheres are about twice as large as the glass spheres coating the surface. This leads to significant slip at the boundary, and the profile is more nearly exponential in this case.

We have also done experiments in a narrow gap geometry, where the shear region is only 4–5-particle diameters thick. In this case, the velocity profile is linear and the temperature is roughly constant across the cell, as shown in Fig. 7.

Fluctuations parallel to the shear are somewhat larger than perpendicular fluctuations. The velocity profile is again independent of shear velocity. The small gap result is consistent with the hydrodynamic model of Sec. V: The uniform rms fluctuations across the gap are accompanied by a linear velocity gradient.

B. Shear forces

The shear stress is found to be roughly independent of shear velocity but to decrease roughly linearly with increasing upward air flow as shown in Fig. 8. The dependence on air flow is consistent with the results by Tardos *et al.* [8] described in Sec. II. Previous experiments [36] showed that the shear stress is directly proportional to the pressure inside

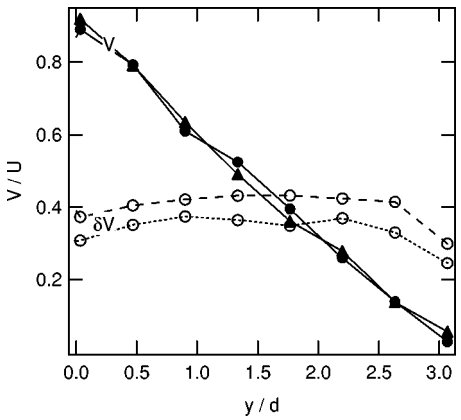

FIG. 7. Velocity profiles (Solid lines) and rms-fluctuation profiles (dashed lines) in a narrow gap geometry with gap width of 4–5 particle diameters. The velocity profile is linear and the rms fluctuation profile is constant. Measurements are made on glass spheres with rotation rates of 0.1 Hz (circles) and 0.02 Hz (triangles), corresponding to $U = 32$ mm/s and 6.4 mm/s.

the granular material. We may therefore assume that air flow decreases the pressure roughly linearly with increasing flow rate.

When there is no air flow, we also find that the shear stress is roughly independent of shear velocity even though stick-slip motion is observed. This indicates that some velocity weakening (i.e., a decrease in shear force with increasing velocity) must occur. The mean shear stress with air flow is a factor of four smaller than the mean shear stress without air flow. For a small gap, the shear force increases with decreasing shear velocity, eventually leading to the jamming of the inner cylinder below a threshold shear velocity.

The air flow at which the transition from stick-slip motion to steady shearing is observed is shown as a function of rotation rate of the cylinder, i.e., of shear velocity, in Fig. 9. We determine the transition from the stick-slip motion to a steady sliding motion from the emergence of a peak at $v = 0$ in the probability distribution of the shear velocity. The critical air flow decreases roughly linearly with rotation rate, i.e., with shear velocity.

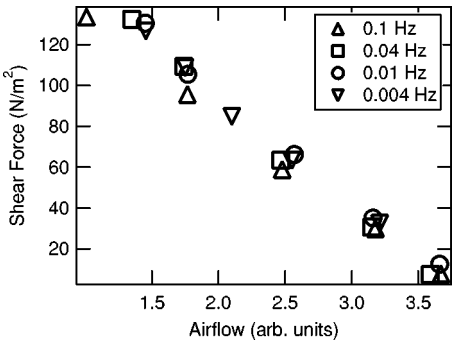

FIG. 8. Mean shear stress vs air flow rate at rotation rates of the cylinder of 0.004, 0.01, 0.04, and 0.1 Hz, corresponding, respectively, (in mm/s) to shear velocities of 1.28, 3.2, 12.8, 32. The shear stress decreases approximately linearly with increasing air flow. The shear stress is independent of shear velocity at most air flows (glass spheres).

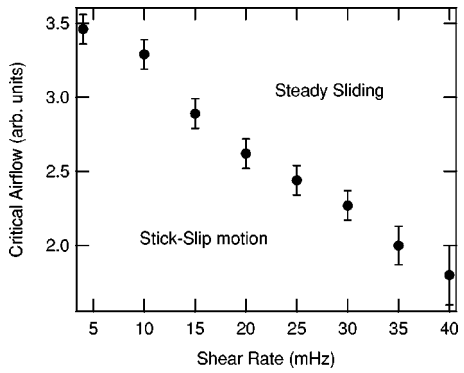

FIG. 9. Air flow at which the transition from stick-slip motion to steady shearing is observed as a function of the rotation rate of the cylinder. The critical air flow decreases roughly linearly with the rotation rate, i.e., with shear velocity (glass spheres).

V. THEORY

A. Hydrodynamic model and main assumptions

Here, we propose a hydrodynamic model for granular flow to describe the data presented in the previous section. By hydrodynamic, we mean that a *local*, mean relationship is assumed to hold between shear stress and shear rate, in contrast to recent approaches that advocate nonlocal relationships (see, e.g., [23], and [1], and references therein). The grains are assumed to behave like inelastic hard spheres, with a diameter d and coefficient of restitution e. We therefore *neglect* any *friction* force between grains. Within this model, collisions between grains are instantaneous. The inelasticity coefficient e is moreover assumed to be independent of the relative velocity of the two colliding particles. Our philosophy is different from that of more sophisticated approaches (such as the simulations of Ref. [37]), where the microscopic model is taken to be as realistic as possible. Here, we deliberately choose the simplest model: our goal is to show that despite its simplicity, a hydrodynamic model leads to many nontrivial results that are usually attributed in the literature to more sophisticated ingredients of granular flow. We check its validity by comparing *a posteriori* our findings to the experimental results. As we demonstrate below, most of the experimental properties of sheared granular flow may be explained by this hydrodynamic, locally Newtonian description of the material.

We consider a simplified Couette geometry: the granular material is confined between two parallel walls, separated by a distance H. The x axis is along the walls, while the y axis is perpendicular to it. The bottom wall, placed at $x=0$, is assumed to move at a velocity U along the x direction and the top wall stays at rest.

We start with the equations of hydrodynamics for the inelastic hard-sphere fluid. Following common practice, we identify the granular temperature with $m[\delta V]^2$, where δV is one component (x or y) of the rms-velocity fluctuation previously defined in Sec. III, and m is the particle mass. There is a small ambiguity in this definition for a sheared granular material since the x and y components of $[\delta V]^2$ (i.e., the components parallel and perpendicular to the flow) differ slightly. However, as may be observed in Fig. 5, they differ only by a scaling factor close to unity. We shall therefore disregard this anisotropy in our theoretical treatment. For the inelastic hard-sphere fluid of local particle density ρ, the equations of hydrodynamics for the mean velocity field V and temperature T may be written as [12]

$$m\rho\left(\frac{\partial V}{\partial t}+V\cdot\nabla V\right)=-\nabla\cdot\sigma \tag{1a}$$

$$m\rho\left(\frac{\partial T}{\partial t}+V\cdot\nabla T\right)=-\boldsymbol{\nabla}\cdot\mathbf{Q}-\sigma:\kappa-\epsilon T, \tag{1b}$$

where : means contraction of the two tensors. In these equations, κ is the symmetrized velocity-gradient tensor

$$\kappa_{\alpha,\beta}=\frac{1}{2}(\partial_\alpha V_\beta+\partial_\beta V_\alpha), \tag{2}$$

σ is the pressure tensor, $\mathbf{Q}$ is the heat flux, and ϵ is the temperature-loss rate per unit volume. As in a Newtonian fluid, we assume a *linear*, *local* relationship between fluxes and forces. We thus write the pressure tensor as

$$\sigma=P\mathbf{I}-2\eta(\kappa-\boldsymbol{\nabla}\cdot V\mathbf{I}), \tag{3}$$

where P is the pressure, η is the shear viscosity, and $\mathbf{I}$ the unit tensor. In a similar way, we assume Fourier's law for the heat flux,

$$\mathbf{Q}=-\lambda\boldsymbol{\nabla}T, \tag{4}$$

with λ the thermal conductivity. These equations are completed by the equation of state of the material, in the form $P=P(\rho,T)$.

In the simplified planar shear cell geometry, the mean flow is a function of y only and parallel to the x direction: $\mathbf{V}=V(y)\mathbf{e}_x$ with $\mathbf{e}_x$ the unit vector in the x direction. From the momentum transport Eq. (1a) in the steady state, one then expects

$$\frac{\partial}{\partial y}\sigma_{yx}=0, \tag{5}$$

$$\frac{\partial}{\partial y}\sigma_{yy}=0. \tag{6}$$

This shows that both the shear stress σ_{xy} $(=\sigma_{yx})$ and the pressure $P=\sigma_{yy}$ are independent of y.

B. Equation of state and high-density expressions for the transport coefficients

In order to solve the hydrodynamic Eqs. (1), explicit expressions for the transport coefficients and the equation of state in terms of density and temperature are needed.

When the system is at rest, the density ρ in the granular material is roughly given by the random close packing (RCP) density ρ_c (the granular system does not crystallize because of a slight polydispersity of the beads). Experimentally, the shear rate is found to dilate the system [11]. More precisely,

the density decrease is larger close to the boundaries, where the shear rate is larger, than far from the moving wall, where the velocity goes to zero [2,37]. As already quoted in Sec. III, our experimental results for the density do qualitatively agree with this observation. Consequently, *a broad range of densities* is explored in the sheared system, going from a value slightly below the RCP density far from the moving wall, down to a density up to 40% less than RCP near the moving wall at high-shear rates. This makes the problem much more difficult than in standard fluids, where the density remains constant over the cell. Here, the functional dependence of the transport coefficients on density is an important ingredient of the theory since it does affect flow properties.

1. Equation of state

For an inelastic hard-sphere system, the equation of state may be written in terms of $g(d)$ the pair-correlation function at contact (d being the diameter) [38,39], in the form

$$P=\rho T\left[1+(1+e)\frac{\pi}{3}\rho d^3 g(d)\right] \tag{7}$$

(ρ is the local numerical density, i.e., the number of particles per unit volume). For both dilute and moderately dense systems ($\rho d^3 \sim 1$), $g(d)$ is accurately described by the Carnahan-Starling formula [38]. However, since the density of the granular material in the shear cell is close to random close packing (RCP) where $g(d)$ diverges, an alternative expression for $g(d)$ is usually assumed [40]:

$$g(d)=\frac{1}{1-\rho/\rho_c}, \tag{8}$$

with ρ_c the density at RCP. The equation of state, Eqs. (7)–(8), then takes the following approximate form in the high-density limit:

$$P=\rho_0\frac{1}{\left(1-\dfrac{\rho}{\rho_c}\right)}T, \tag{9}$$

with $\rho_0=(1+e)(\pi/3)\rho_c^2 d^3$. The equation of state thus gives a natural link between temperature and density: since the pressure is independent of y, one obtains

$$1-\frac{\rho}{\rho_c}=\frac{\rho_0}{P}T. \tag{10}$$

This equation shows that the regions of small temperature correspond to high-density regions, $\rho \sim \rho_c$, and vice versa.

2. Transport coefficients

Expressions for the transport coefficients of the inelastic hard-sphere model have been computed from the Enskog equation [12,39]. This kinetic equation takes the effects of excluded volume into account, but it neglects any correlation between the velocities of colliding particles. This approach yields expressions for the transport coefficients in terms of the density, temperature, and pair-correlation function at contact. We refer to Refs. [12,39] for explicit expressions. We note that *in the high-density limit*, $g(d)$ becomes very large and the dependence of the Enskog transport coefficients on density mainly come from the terms proportional to $g(d)$. In this case, the transport coefficients reduce to the generic forms

$$\eta_E(\rho,T)\simeq\eta_0\frac{m^{1/2}}{d^2}g(d)T^{1/2},$$

$$\lambda_E(\rho,T)\simeq\lambda_0\frac{1}{m^{1/2}d^2}g(d)T^{1/2},$$

$$\epsilon_E(\rho,T)\simeq\epsilon_0\rho\frac{1}{m^{1/2}d}g(d)T^{1/2}, \tag{11}$$

where m is the mass of the particles and η_0, λ_0, ϵ_0 are dimensionless coefficients that depend only slightly on density in the high-density limit. If $\rho\sim\rho_c$ as discussed above, these coefficients may be taken as numerical constants. Finally, we mention that ϵ_0 is proportional to $1-e^2$, where e is the coefficient of restitution. Thus, $\epsilon_0=0$ in the purely elastic case, as expected.

The full expressions for the transport coefficients obtained within the Enskog kinetic theory have been found in simulations to be correct for small and intermediate densities [27]. However, as mentioned above, the density of the flowing material in the shear cell is higher and close to the RCP density. In this limit, some of the Enskog expressions for the transport coefficients may no longer be valid, mainly because correlations between colliding particles and collective phenomena, which are not included in the Enskog theory, then play an important role. The reason is quite intuitive: at high density close to random close packing, a particle may move substantially (over a distance of the order of its diameter) only if its neighbors move coherently. Only collective motion is therefore possible. It has been found in molecular-dynamics simulations of the hard-sphere model [27] that these correlations only affect the shear viscosity and self-diffusion coefficient, which depart from their Enskog approximation at high densities. On the other hand, the thermal conductivity has been found to be well described by the Enskog expression up to very high densities. Such behavior is in fact expected since transport of energy does not require motion of particles over large distances (only ''rattling'' around the mean position is involved in energy transport). Similar conclusions were reached by Leutheusser [28] on the basis of a mode-coupling calculation for the elastic hard-sphere model.

As a result of these considerations, the thermal conductivity λ and loss rate ϵ are expected to keep their Enskog expressions λ_E and ϵ_E, as given in Eqs. (11), over the whole range of densities (between intermediate densities up to RCP)

$$\lambda(\rho,T)\simeq\lambda_0\frac{1}{m^{1/2}d^2}\frac{1}{\left(1-\frac{\rho}{\rho_c}\right)}T^{1/2},$$

$$\epsilon(\rho,T)\simeq\epsilon_0\frac{1}{m^{1/2}d}\frac{\rho_c}{\left(1-\frac{\rho}{\rho_c}\right)}T^{1/2}. \tag{12}$$

On the other hand, a crossover is expected for the shear viscosity between its Enskog approximation in Eq. (11) for intermediate densities, towards an asymptotic stronger divergence as a function of density very close to RCP. Such a crossover is indeed found in molecular-dynamics calculations of the self-diffusion coefficient in a monodisperse hard-sphere system close to freezing [41]. By analogy with the behavior of supercooled liquids above the glass transition [42], we shall assume that very close to RCP, the viscosity diverges *algebraically* as a function of density ρ near ρ_c

$$\eta(\rho,T)\sim\frac{\eta_1}{\left(1-\frac{\rho}{\rho_c}\right)^{\beta}}\frac{m^{1/2}}{d^2}T^{1/2}. \tag{13}$$

Here, η_1 is a dimensionless numerical constant. At this point, the exponent β is a phenomenological parameter in the theory. Since the viscosity is expected to diverge more strongly than its Enskog expression, we expect β to be larger than one. We shall discuss in the next section how the form proposed in Eq. (13) compares with the experimental results.

We emphasize again that such an algebraic divergence of the viscosity is expected in supercooled liquids close to the glass transition [42]. More precisely, an algebraic divergence is associated with the existence of cooperative interactions that predominate over thermally activated processes [42]. The functional form in Eq. (13) is predicted by mode-coupling calculations of the dynamics of supercooled liquids. In the case of a 3D hard sphere, the latter approach yields an exponent $\beta=2.58$ [43].

To our knowledge, there is no expression for the viscosity over a full range of densities that would make explicit the crossover between the Enskog expression at intermediate densities and the asymptotic expression at very high densities. In order to avoid restrictive assumptions about the general form of the density dependence of the viscosity, we shall write, in general,

$$\eta(\rho,T)=\overline{\eta}(\rho)\frac{m^{1/2}}{d^2}T^{1/2}, \tag{14}$$

where the function $\overline{\eta}(\rho)$ has the two limiting forms

$$\rho\sim d^{-3}<\rho_c\qquad\overline{\eta}(\rho)\simeq\frac{\eta_0}{\left(1-\frac{\rho}{\rho_c}\right)},$$

$$\rho\sim\rho_c\qquad\overline{\eta}(\rho)\sim\frac{\eta_1}{\left(1-\frac{\rho}{\rho_c}\right)^{\beta}}. \tag{15}$$

As we shall show in the following sections, the knowledge of these two limiting behaviors is sufficient to obtain a quantitative description of the flow and a qualitative picture for the shear forces.

Combining Eqs. (9) and (12) allows us to write the transport coefficients in terms of the pressure and temperature as

$$\eta(\rho,T)\simeq\frac{m^{1/2}}{d^2}\overline{\eta}\left(\frac{\rho_0 T}{P}\right)T^{1/2}, \tag{16}$$

$$\lambda(\rho,T)\simeq\lambda_0\frac{1}{m^{1/2}d^2}\frac{P}{\rho_0 T^{1/2}}, \tag{17}$$

$$\epsilon(\rho,T)\simeq\epsilon_0\frac{1}{m^{1/2}d}\frac{P}{T^{1/2}}. \tag{18}$$

(Note that in order to improve readability, we dropped a numerical constant prefactor ρ_c/ρ_0 in the expression for ϵ, which amounts to a rescaling of the numerical prefactor ϵ_0.)

C. rms and mean flow velocity profiles

In this section, we compute the granular temperature profile $T(y)$ and mean-velocity profile $V(y)$. In the stationary Couette geometry, the hydrodynamic equation for $T(y)$ is found to reduce to

$$\frac{\partial}{\partial y}\lambda(\rho,T)\frac{\partial}{\partial y}T+\sigma_{xy}\dot{\gamma}-\epsilon(\rho,T)T=0, \tag{19}$$

and

$$\sigma_{xy}=\eta(\rho,T)\dot{\gamma}=\text{const.}, \tag{20}$$

where $\dot{\gamma}=dV_x(y)/dy$ is the shear rate. Using the expression for the shear stress, $\sigma_{xy}=\eta(\rho,T)\dot{\gamma}$, the second term of Eq. (19) may be rewritten as $\sigma_{xy}\dot{\gamma}=\sigma_{xy}^2/\eta(\rho,T)$. Note that σ_{xy} is negative because $\dot{\gamma}=\partial v_y/\partial x$ is negative throughout the sample.

Both equations involve the explicit form of the density dependence of the viscosity $\eta(\rho,T)$, for which no explicit functional form is available to us. At first sight, it would seem hopeless to obtain a full expression of the temperature and velocity profiles. This is not the case. As we shall show, a simple phenomenological picture, which emerges from the asymptotic forms of $\eta(\rho,T)$ as given in Eq. (15), allows one to overcome this problem and to obtain tractable expressions for the temperature and mean velocity.

We proceed in two steps. First, we describe this phenomenological ''two-region'' picture and obtain expressions for the velocity and temperature profile. Then, in a second step, we come back to a more general but formal solution of Eqs.

(19) and (20) (in the next section). This general discussion allows us to discuss the velocity dependences of the shear forces.

We start with the discussion of the temperature profile. The role of the the nonlinear term $\sigma_{xy}\dot{\gamma}$ in Eq. (19) is in fact physically quite simple to understand. It merely acts as a source (''heating'') term for the fluctuations: it is through this nonlinear contribution that the flow creates the fluctuations that couple back to the mean flow. However, this source term is only effective close to the wall as we show below. This simplifies considerably the picture for the creation and transport of temperature. Basically, two regions can be treated separately: close to the moving boundary, fluctuations are ''created'' through the nonlinear coupling to the flow; far from the boundaries, inelastic dissipation dominates over nonlinear heating, and the local temperature profile is determined entirely by the diffusion and heat-loss terms of Eq. (19).

This separation may be understood on the basis of the asymptotic behavior of the viscosity discussed above. Indeed, it is easy to show that far from the wall, the nonlinear term $\sigma_{xy}\dot{\gamma}$ goes to zero faster than the dissipation term $\epsilon(\rho,T)T$ in Eq. (19). Away from the moving boundary, the temperature goes to zero and the density goes accordingly towards RCP. From Eqs. (15) and (18), it follows that the nonlinear term behaves in this region similar to $\sigma_{xy}^2/\eta(\rho,T)\propto T^{(2\beta-1)/2}$, while the dissipative term in this region scale with temperature as $\epsilon(\rho,T)T\propto T^{1/2}$ [where Eq. (18) has been used]. Since we anticipated that the exponent β is larger than one (around 1.75 as found experimentally, see below), the nonlinear term decays more strongly towards zero than the dissipative one. On the other hand, the nonlinear term is relevant close to the moving boundary where the shear rate is large (or equivalently, the density is smaller). We note that if the exponent β had been equal to one, both previous terms would have been comparable and then the picture of two separate regions would not have been appropriate.

Close to the walls, the full nonlinear equation including the ''heating'' term should be solved. This is in fact not necessary to make simple predictions for the rms- and mean-velocity profiles. An inspection of the experimental profiles, as presented in Fig. 3, shows that in the region close to the moving boundary, the temperature is roughly constant over a small layer, several-particle diameters thick, with a thickness that may be considered in a first approximation to be independent of the shearing velocity U. As a first step, we therefore assume in an *ad hoc* way that for distances y smaller than a cutoff distance y_w, the temperature T is constant, $T(y)=T_0$. In this pictorial view, the boundary layer corresponds to the region where the nonlinear term is important. At this stage, the parameter T_0 merely plays the role of a normalizing constant. We shall come back to this point in much more detail in the discussion of the shear forces because, while the precise value of T_0 does not influence the velocity profile, it does strongly affect the prediction for the shear forces.

We are now in a position to obtain an explicit expression for the temperature profile. For distances larger than y_w, the transport equation for the temperature Eq. (19) reduces to

$$\frac{\partial}{\partial y}\left\{\lambda_0\frac{1}{m^{1/2}d^2}\ \frac{P}{\rho_0 T^{1/2}}\frac{\partial}{\partial y}\right\}T-\epsilon_0\frac{1}{m^{1/2}d}PT^{1/2}=0, \quad (21)$$

where the high-density expressions for the transport coefficients Eqs. (18) has been used.

As shown previously, the pressure P is independent of y, so one may rewrite Eq. (21) as

$$\frac{\partial^2}{\partial y^2}T^{1/2}-\frac{1}{\delta^2}T^{1/2}=0, \quad (22)$$

where δ has the dimension of a length and is defined as

$$\delta^2=\frac{2\lambda_0}{\epsilon_0\rho_0\ d}. \quad (23)$$

The parameters λ_0 and ϵ_0 are just numerical constants in the high-density regime of interest to us. Therefore, one expects δ to be of the order of a few-particles diameters. Note that since ϵ_0 is proportional to $1-e^2$ (with e the restitution coefficient), the decay length δ goes to infinity when the system become perfectly elastic, as one would expect. This equation has to be completed by boundary conditions for the temperature at both walls. At the moving wall, we set $T(y)=T_0$ for $y<y_w$, as discussed above. At the wall at rest, detailed experiments, as shown in Fig. 4, show that the temperature profile is compatible with a vanishing heat-flux condition $dT/dy=0$. (In general, one expects the boundary condition for the temperature to relate the heat flux at the boundary to the product of the interface [Kapitza] resistance and the temperature jump: Here, we just assume that the Kapitza resistance is very small. We shall come back to this point in the next section.)

The solution of Eq. (22) with these boundary conditions is

$$y<y_w, \quad T(y)=T_0, \quad (24)$$

$$y_w<y, \quad T^{1/2}(y)=T_0^{1/2}\frac{\cosh\left(\frac{H-y}{\delta}\right)}{\cosh\left(\frac{H-y_w}{\delta}\right)}. \quad (25)$$

In this equation, H is the thickness of the shear cell. As shown in Fig. 3, this result is in good agreement with the experimental data. We find that $\delta=4.7d$ and $y_w=2.8d$ for glass spheres, but these parameters depend somewhat on the material properties.

The mean-velocity profile can be obtained along the same lines from the temperature profile of Eq. (25). Equation (20) gives unambiguously the shear rate $\dot{\gamma}$ in terms of the temperature profile $T(y)$, since the y dependence of the density is already contained in the temperature through the equation of state, Eq. (10). It seems at first sight difficult to make an explicit prediction for the velocity profile, since the explicit

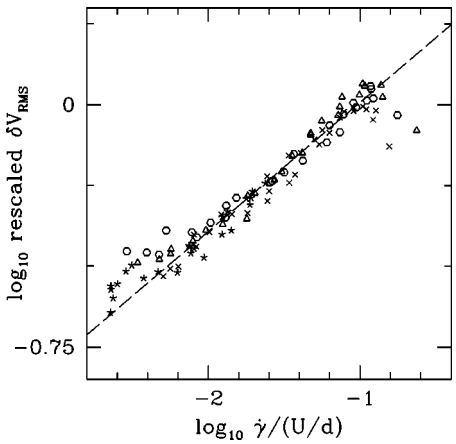

FIG. 10. Connection between the local rms-velocity fluctuations and local shear rate (same symbols as for Fig. 2). Local fluctuations are found to increase approximately as a power law of the local velocity gradient, with a power of 0.4 (dashed line).

expression of the viscosity is not known over the full range of densities. However, the ''two regions'' picture, which emerged in the discussion of the temperature profile, is relevant for the mean-velocity profile, as well. Far from the wall (i.e., for $y>y_w$), the temperature decays to zero and the density goes accordingly to the RCP limit [as shown in Eq. (10)]. In this region, one thus expects an ''anomalous'' scaling for the density dependence of the viscosity, according to Eq. (15). Thus, one finds for $y>y_w$

$$\eta_0 \frac{m^{1/2}}{d^2}\left(\frac{P}{\rho_0 T}\right)^{\beta} T^{1/2}\dot{\gamma}=\sigma_{xy}. \tag{26}$$

It is interesting to note that this relation yields a scaling relationship between the temperature T and $\dot{\gamma}$ that can be tested experimentally. The previous equation may be rewritten in the form

$$\dot{\gamma}=\left\{\frac{\sigma_{xy}}{\eta_0 \frac{m^{1/2}}{d^2}\left(\frac{P}{\rho_0}\right)^{\beta}}\right\} T^{1/2(2\beta-1)}. \tag{27}$$

This power-law relationship has been checked experimentally, as shown in Fig. 10, where the local rms-velocity profile $\delta V \equiv (T/m)^{1/2}$ is plotted versus the local velocity gradient dV_x/dy on logarithmic scales.

In this plot, a scaling exponent $\alpha=0.4$ is obtained for the glass bead system. This allows for an experimental determination of the exponent β for the ''anomalous'' divergence of the viscosity close to RCP. According to Eq. (27), α is identified in the theory as $\alpha=1/(2\beta-1)$, so that $\beta\cong 1.75$. The fact that this exponent exceeds unity seems to confirm the collective character of the dynamics in the granular material. However, we caution that the fluctuations could be underestimated (see Sec. III B), causing the relationship in Fig. 10 to be affected to an extent that is hard to estimate. This value of the exponent is slightly smaller than the previously mentioned result for $\beta=2.58$ obtained within the mode-coupling theory applied to the case of hard spheres [43]. A possible reason for this difference could lie in the rotational degrees of freedom of the beads in the experimental system that are absent from the mode-coupling estimate. By increasing the number of degrees of freedom, an effective decrease of the shear viscosity could be obtained. We leave this question for further investigation.

We emphasize that the observation of the scaling relationship between $\dot{\gamma}$ and $T^{1/2}$ is not restricted to our system. We have applied the same procedure to the data of Howell *et al.* [44], which were obtained in a 2D system of photoelastic disks: for the 14 different densities studied in this paper, a similar scaling relationship between the local δV_{rms} and $\dot{\gamma}$ is measured. An exponent $\alpha\sim 0.5$ is obtained, yielding $\beta\sim 1.5$ for that experiment. Moreover, both the mean and fluctuation profiles obtained by Howell *et al.* can be fitted within the present paper. This observation seems to indicate that the coupling between mean and rms fluctuations, which is the essence of our model is a general feature of the underlying dynamics of the granular material.

Once the exponent β is determined, the velocity profile may be obtained by integration. In the boundary layer for the temperature ($y<y_w$), the temperature is assumed to be a constant; Eq. (20) then shows that the shear rate is constant, yielding a linear velocity profile. This observation is in agreement with the experimental velocity profiles, as can be seen by a careful inspection of Fig. 2 for $y<y_w$. On the other hand, for $y>y_w$, the velocity profile is obtained by integrating Eq. (27) together with the solution (25) for the temperature profile. The full velocity profile is obtained by matching the two solutions at y_w (where we assume continuity of velocity and shear rate). The solution obeying no-slip boundary conditions at both walls takes the form

$$V_x(y)=U\left(1-\frac{\int_0^y dy'\,\phi(y')}{\int_0^H dy'\,\phi(y')}\right), \tag{28}$$

where the function $\phi(y)$ is defined as

$$y<y_w, \quad \phi(y)=1, \tag{29}$$

$$y>y_w, \quad \phi(y)=\left[\frac{\cosh\left(\frac{H-y}{\delta}\right)}{\cosh\left(\frac{H-y_w}{\delta}\right)}\right]^{2\beta-1}. \tag{30}$$

When the value $\beta=1.75$ previously obtained for the exponent β is used, the theoretical velocity profile defined in Eqs. (28) and (30) is easily integrated numerically. The result is plotted in Fig. 2 together with the experimental results. As can be seen, good agreement is obtained with the theory.

Although the two-region picture seems to be quite successful in describing the mean- and rms-velocity profiles, it would be more satisfactory to have a full expression of the density dependence of the viscosity over the full range of densities in order to integrate Eqs. (19) and (20) explicitly.

The two-region picture is to be considered merely as a simple and physically sound way of dealing with our ignorance of the explicit functional dependence of the viscosity on density. Its success indicates that the velocity profile does not depend crucially on the details of this relationship.

D. Towards "solidlike" shear forces

1. General discussion

In his pioneering work, Bagnold measured the shear force in a Couette cell and found a quadratic increase of the shear force as a function of the shearing velocity $\sigma_{xy} \propto U^2$ [11]. Using kinetic arguments, he proposed a phenomenological relationship between shear stress and shear rate in the form $\sigma_{xy} \propto \dot{\gamma}^2$, which may be understood by assuming that the collision frequency between granular particles is fixed by the shear rate $\dot{\gamma}$ itself. Subsequent experiments were performed [8], which showed that the functional dependence of the shear force as a function of the shearing velocity does depend on whether the system is allowed to dilate or not: when the system is sheared at constant volume, the shear force is found to be proportional to U^2 (i.e., the Bagnold scaling); when the system is allowed to dilate, the shear force is found to be independent of U. In the present geometry, the material is allowed to dilate and a solidlike friction force, i.e., approximate independence of U, is found.

It is tempting to ascribe the solidlike behavior to a solid friction force existing between granular particles at contact. On the other hand it is difficult to reconcile this behavior with constant-volume Bagnold scaling, $\sigma_{xy} \propto U^2$, whose origin is purely kinetic. Here, we shall show that both behaviors may be accounted for within the hydrodynamic model we have introduced.

Constant volume results: It is evident that the Bagnold scaling, $\sigma_{xy} \propto U^2$, originates from a general dimensional argument, whatever the local relationship between shear stress and shear rate is: In other words, the *global* scaling $\sigma_{xy} \propto U^2$ obtained in a constant volume experiment does not necessary imply that the *local* relationship is $\sigma_{xy} \propto \dot{\gamma}^2$. The reason is very simple. Let us consider a system of N inelastic hard spheres contained in a plane Couette cell of (fixed) volume V. The bottom boundary is moving at a constant velocity U, while the upper boundary stays at rest.

In this case, the only microscopic velocity scale entering the dynamics is U, the velocity of the moving wall. In other words, *all dynamical quantities* may be written in terms of the shear velocity U only, which fixes the only time scale in the problem. From the analysis of the full N-body dynamics, one thus concludes in general that

$$\frac{V_x(y)}{U} = f\left(\frac{y}{d}, \frac{N}{V}, \frac{H}{d}\right),$$

$$\frac{T(y)}{mU^2} = g\left(\frac{y}{d}, \frac{N}{V}, \frac{H}{d}\right),$$

$$P = \frac{N}{V} p\left(\frac{N}{V}, \frac{H}{d}\right) mU^2,$$

$$\sigma_{xy} = \frac{N}{V} \sigma_0\left(\frac{N}{V}, \frac{H}{d}\right) mU^2, \tag{31}$$

where f, g, p, σ_0 are dimensionless functions; H is the cell width and d the bead diameter.

In this context, the Bagnold scaling results naturally from the last equality in Eq. (31), *whatever the relationship between* σ_{xy} *and* $\dot{\gamma}$ *is*. The only important condition is that the microscopic dynamics of the granular material only involve binary collisions.

Constant pressure results: Experiments performed in a constant pressure situation are more subtle to handle. The introduction of a constant pressure in the system introduces a time scale, namely $(m/Pd)^{1/2}$, which will compete with the time scale associated with the shearing velocity, d/U. Thus, different regimes might be found depending on whether the time scale associated with the shear velocity is larger or smaller than the one associated with pressure.

We show in the following that in the situation of constant pressure, a shear force independent of shear velocity is obtained at large shearing velocity, while a velocity weakening regime is found at small velocities.

2. Shear forces at constant pressure from the hydrodynamic model: Qualitative

In the previous section, the experimental mean- and rms-velocity profiles were reproduced by using a simple ''two-regions'' picture, which allowed us to overcome our lack of knowledge of the full functional dependence of the viscosity on the density. However, the shear force originates in the interaction between the wall and the fluid particles adjacent to it. Therefore, one needs a good description of the region close to the wall in order to get valuable information about the shear forces. This requires a careful analysis of the nonlinear ''heating'' term in the equation for the temperature, Eq. (19), which we perform in this section.

We first present an approximate, qualitative argument that helps explain physically what quantities control the friction force in the shearing experiment. We then present the full approach, which clarifies the crude approximations made in the qualitative arguments.

The shear force is defined in the hydrodynamics model as the viscosity times the shear rate, both evaluated *at the boundary*. Using the expression for the viscosity, Eq. (14), this yields

$$\sigma_{xy} = \overline{\eta\left(\frac{\rho_0 T_0}{P}\right)} \frac{m^{1/2}}{d^2} T_0^{1/2} \dot{\gamma}\Big|_0 . \tag{32}$$

We need a second equation giving the temperature at the boundary T_0. In the ''two-regions'' picture we introduced above, the temperature is created near the boundary and then transported to the rest of the system In this picture, the temperature T_0 merely comes from a balance between the dissipation rate close to the moving boundary $-\epsilon T_0$ and the ''heating term,'' $\sigma_{xy}\dot{\gamma}|_0$. Together this gives

$$\sigma_{xy}\dot{\gamma}|_0 \simeq \frac{\epsilon_0}{m^{1/2}d} P T_0^{1/2}, \tag{33}$$

where we have used the expression in Eq. (18) for the dissipation rate ϵ.

The shear rate $\dot{\gamma}|_0$ may be eliminated from the two previous equations, Eqs. (32) and (33), to give

$$\frac{\sigma_{xy}}{P} \simeq \left[\frac{\epsilon_0}{\rho_0 d^3} \overline{\eta}\left(\frac{\rho_0 T_0}{P} \right) \frac{\rho_0 T_0}{P} \right]^{1/2}. \tag{34}$$

Now, depending on the ratio $\rho_0 T_0/P$, two limiting behaviors are obtained:

(i) If $\rho_0 T_0/P$ is large, then the viscosity takes its intermediate density expression in Eq. (15), $\overline{\eta}(\rho_0 T_0/P) \simeq \eta_0 P/\rho_0 T_0$. In this limit, one then obtains from Eq. (34)

$$\sigma_{xy} \simeq \mu_0 P, \tag{35}$$

with $\mu_0 = \epsilon_0 \eta_0/\rho_0 d^3$ a dimensionless constant. In other words, the shear force is expected to be independent of the shear rate and proportional to pressure, as is usually found in solid friction.

(ii) If $\rho_0 T_0/P$ is small, then the viscosity takes its high density expression in Eq. (15), $\overline{\eta}(\rho_0 T_0/P) \simeq \eta_1 (P/\rho_0 T_0)^{\beta}$ and Eq. (34) gives

$$\frac{\sigma_{xy}}{P} \simeq \left[\frac{\epsilon_0 \eta_1}{\rho_0 d^3} \left(\frac{P}{\rho_0 T_0} \right)^{\beta - 1} \right]^{1/2}. \tag{36}$$

The temperature T_0 enters explicitly in this formula. It has to be obtained as a function of the shearing velocity U. This may be accomplished using the energy balance discussed above, which results in Eq. (33). In this equation, one expects the shear rate at the boundary to be roughly given by $\dot{\gamma}|_0 \sim U/\ell_0$, where ℓ_0 is a distance typically of the order of a few diameters (this point is confirmed in the full discussion to follow). One thus gets

$$T_0^{1/2} \sim \frac{\sigma_{xy}}{P} \frac{d}{\ell_0} m^{1/2} U, \tag{37}$$

which still depends on the ratio between shear stress σ_{xy} and pressure P. Combining this expression for T_0 as a function of U and σ_{xy}/P and the formula for σ_{xy}/P as a function of T_0 in Eq. (36) yields the final result

$$\sigma_{xy} \simeq \mu_1 P \left(\frac{\rho_0 m U^2}{P} \right)^{1 - \beta/2\beta}, \tag{38}$$

where we have introduced the dimensionless constant, $\mu_1 = [\epsilon_0 \eta_1/\rho_0 d^3 (d/\ell_0^{1-\beta})^{1-\beta}]^{1/2\beta}$.

The crossover between the two regimes occurs at the "critical" velocity U_c defined as $U_c \sim (P/m\rho_0)^{1/2}$.

3. Shear forces: Quantitative

These results obtained from the arguments of Sec. V D 2 are in fact fully confirmed by a more detailed and careful analysis of the nonlinear set of equations for temperature and velocity, Eqs. (19) and (20). Here we present the full analysis. In order to simplify the discussion, we assume that the granular material is semi-infinite, ı.e., the cell width H is larger than the decay length for temperature δ defined in Eq. (23).

We proceed in two steps. First, we obtain two closed implicit equations for the temperature at the boundary (T_0) and the shear stress σ from an analysis of Eqs. (19) and (20). These equations are written in terms of the general form of the viscosity, Eq. (14). Then in a second step, we discuss the different limiting behavior for the shear stress as a function of the shear velocity U ("large" and "small" velocities).

(a) First condition defining T_0 and σ_{xy}: We first rewrite the full temperature equation Eq. (19), in terms of the expressions for the transport coefficients Eqs. (14) and (12),

$$\frac{\partial}{\partial y}\left\{ \frac{\lambda_0}{m^{1/2}d^2} \frac{P}{\rho_0 T^{1/2}} \frac{\partial}{\partial y} \right\} T + \frac{\sigma_{xy}^2}{\overline{\eta}(\rho) \dfrac{m^{1/2}}{d^2} T^{1/2}} - \epsilon_0 \frac{1}{m^{1/2}d} P T^{1/2} = 0, \tag{39}$$

which can be rewritten as

$$\frac{\partial^2}{\partial y^2} T^{1/2} + \frac{T_s}{\delta^2 \overline{\eta}(\rho) T^{1/2}} - \frac{1}{\delta^2} T^{1/2} = 0, \tag{40}$$

where we have introduced $T_s = \delta^2 \sigma_{xy}^2 \rho_0 d^4/(2\lambda_0 P)$, a quantity with the dimension of a temperature; It may be rewritten more conveniently as $T_s = (P/\rho_0)(\sigma_{xy}/P)^2 (\rho_0 d^3/\epsilon_0)$, if we use the explicit expression of δ, which has been given in Eq. (23). It is important to note that the term $\overline{\eta}[\rho(y)]$ is a function of $T(y)$ only through the equation of state, Eq. (9). Let us introduce $u = (T/m)^{1/2}$, which has the dimension of a velocity. A first integral of Eq. (39) may be obtained using a standard recipe of classical mechanics: we multiply Eq. (39) by du/dy and integrate over u. We obtain

$$\frac{1}{2}\left(\frac{du}{dy} \right)^2 + \int_0^u du' \frac{T_s}{m\delta^2} \frac{1}{\overline{\eta}(\rho_0 m u'^2/P) u'} - \frac{1}{2\delta^2} u^2 = E. \tag{41}$$

Note that the density dependence of $\overline{\eta}(\rho)$ has been rewritten in terms of its dependence on $u = (T/m)^{1/2}$ thanks to the equation of state Eq. (10). The parameter E is a constant, which in the mechanical analogy, fixes the "energy" of the system. We now introduce the effective "potential" $V(u)$ defined as

$$V(u) = \int_0^u du' \frac{T_s}{m\delta^2} \frac{1}{\overline{\eta}(\rho_0 m u'^2/P) u'} - \frac{1}{2\delta^2} u^2, \tag{42}$$

which allows us to rewrite Eq. (41) as

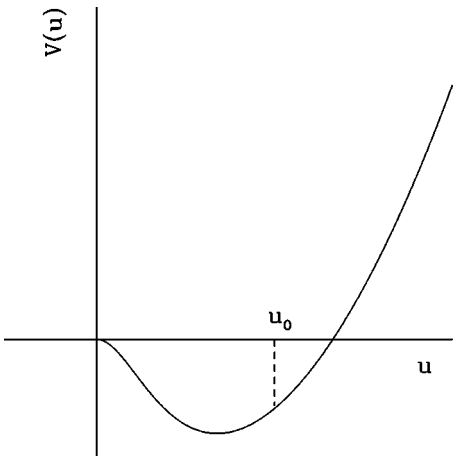

FIG. 11. Typical behavior of the potential $V(u)$ as a function of u.

$$\frac{1}{2}\left(\frac{du}{dy}\right)^2 + V(u) = E. \tag{43}$$

The behavior of the potential $V(u)$ can be obtained by analyzing the two limits $u \to 0$ and $u \to \infty$. The limit $u \sim 0$ corresponds to small temperature, i.e., densities close to RCP. According to the expression of the viscosity close to RCP, Eq. (15), the first term in the potential in Eq. (42) behaves in this limit similar to

$$\int_0^u du' \frac{T_s}{m\delta^2} \frac{1}{\overline{\eta}(\rho_0 m u'^2/P)u'} \simeq \frac{T_s d^2}{\eta_1 m 3/2\delta^2}\left(\frac{\rho_0 m}{P}\right)^{\beta} \int_0^u du' u'^{2\beta-1} \propto u^{2\beta}. \tag{44}$$

This term vanishes more rapidly than the last, quadratic term of $V(u)$ (since the exponent verifies $\beta > 1$). Therefore, close to $u \sim 0$, one has $V(u) \simeq -(1/2\delta^2)u^2$.

In the limit of large u, i.e., high temperature and intermediate density, the integral term in $V(u)$ behaves as

$$\int_0^u du' \frac{T_s}{m\delta^2} \frac{1}{\overline{\eta}(\rho_0 m u'^2/P)u'} \simeq \int_0^u du' \frac{\rho_0 T_s}{\eta_0 P \delta^2} u' = \frac{\rho_0 T_s}{\eta_0 P} \frac{u^2}{2\delta^2}, \tag{45}$$

which, when combined with the second term in Eq. (42), gives

$$V(u) = \left[\frac{\rho_0 T_s}{\eta_0 P} - 1\right] \frac{u^2}{2\delta^2}. \tag{46}$$

Thus, depending on the sign of the first factor on the right had side of the equation, $V(u)$ goes to plus or minus infinity when $u \to \infty$. In Fig. 11, we have arbitrarily chosen a positive sign to emphasize the different behavior of $V(u)$ in the different limits, but the discussion does not depend on this particular choice.

The "energy" E in Eq. (41) may be computed from the boundary conditions. As already mentioned, we assumed a semi-infinite system in this section to simplify the discussion. At infinity, both the temperature and its gradient are expected to vanish, and so does u: $du/dy \to 0$ and $u \to 0$. Consequently, the "energy" E is obtained to be zero: $E = 0$. This imposes the temperature at the boundary, $T_0 = m u_0^2$, which has to satisfy

$$\frac{1}{2}\left(\frac{du}{dy}\right)^2\bigg|_{y=0} + V(u_0) = 0. \tag{47}$$

As we mentioned briefly in Sec. V C, one expects, in general, that the boundary condition for the temperature relates the temperature gradient to the temperature at the boundary, in the form

$$J_Q = -\kappa \frac{dT}{dy}\bigg|_{y=0} = R_K T|_{y=0}, \tag{48}$$

where R_K is a phenomenological parameter, usually denoted as the Kapitza resistance. The ratio $\ell_K = \kappa/R_K$ has the dimension of a length. Following the same arguments that led us to the expression of the thermal conductivity, Eq. (18), R_K is expected to be proportional to the fluid-wall collision frequency, i.e., to $P/[\rho_0 T^{1/2}(y=0)]$. The length ℓ_K is thus expected to be independent of pressure, and only fixed by the "microscopic" quantities such as the diameter of the particles and the roughness of the walls. Rewriting Eq. (48) in terms of the field u, we find the condition for the temperature at the boundary

$$\frac{1}{2\ell^2} u_0^2 + V(u_0) = 0, \tag{49}$$

with $\ell = 2\ell_K$. Using Eq. (42) for $V(u)$, we obtain

$$\frac{1}{2}\left(\frac{1}{\ell^2} - \frac{1}{\delta^2}\right) u_0^2 + \int_0^{u_0} du \frac{T_s}{m\delta^2} \frac{1}{\overline{\eta}(\rho_0 m u^2/P)u} = 0, \tag{50}$$

where we recall that $T_0 = m u_0^2$ and $T_s = (P/\rho_0)(\sigma_{xy}/P)^2(\rho_0 d^3/\epsilon_0)$.

It is interesting to note that, since the second term in Eq. (50) is positive, the first term has to be negative, so that $\ell > \delta$. In the opposite case, the only allowed solution to Eq. (50) is $T_0 = 0$, i.e., no temperature is introduced in the system. This condition is in some sense expected: if ℓ goes to zero, the boundary condition for the temperature at the wall Eq. (48) imposes $T_0 = 0$, so that no temperature may be introduced in the system. Physically, ℓ is related the amount of energy input at the boundary, while δ has to do with the dissipation [see Eq. (23)], so the condition $\ell > \delta$ may be understood as an energy balance condition: if not enough energy is introduced in the system at the boundary, the dissipation is too strong to allow flow.

(b) Second condition defining T_0 and σ_{xy}: A second condition relating σ_{xy} and T_0 may be obtained by formally integrating the momentum equation (20):

$$V_x(y) = U - \int_0^y \frac{|\sigma_{xy}|}{\eta(\rho,T)} dy', \tag{51}$$

where we used the fact that $\sigma_{xy}<0$ to replace σ_{xy} by $-|\sigma_{xy}|$. As $y\to\infty$, the velocity goes to zero, so one gets the condition

$$U = \int_0^\infty \frac{|\sigma_{xy}|}{\eta(\rho,T)} dy'. \tag{52}$$

The explicit form of the y dependence of density and temperature is not known explicitly, but may be obtained formally from the first integral obtained previously, Eq. (41) (with $E=0$). The latter yields an implicit condition for the field u as

$$dy = -\frac{du}{\sqrt{-2V(u)}}, \tag{53}$$

which allows us to rewrite the second condition Eq. (52), in terms of $\eta(\rho,T)$ only

$$U = \frac{|\sigma_{xy}|d^2}{m} \int_0^{u_0} \frac{1}{\overline{\eta}(\rho_0 m u^2/P) u} \frac{du}{\sqrt{-2V(u)}}, \tag{54}$$

where the potential $V(u)$ is given in Eq. (42).

The two equations Eqs. (50) and (54) in principle allow both T_0 and σ_{xy} to be determined in terms of the pressure P and velocity U.

(c) Limiting behaviors of the shear forces: Two limits of the previous equations may be discussed for large and small shear velocity limit U (we shall specify below what we mean by ''large'' and ''small'').

(i) Large velocity limit: Let us assume that the temperature at the boundary T_0 satisfies $T_0 > P/\rho_0$. This corresponds to the large velocity limit. In this case, the density close to the wall is intermediate and the shear viscosity takes its Enskog asymptotic expression, as quoted in Eqs. (14) and (15): $\overline{\eta}(\rho_0 m u^2/P) \simeq P/\rho_0 m u^2$.

In Eq. (50), corresponding to the first condition, the integral is dominated by its large u behavior, where the function $\overline{\eta}$ behaves similar to $\overline{\eta}(\rho_0 m u^2/P) \simeq (P/m\rho_0) u^{-2}$. To a good approximation, the first condition then takes the asymptotic form

$$\frac{1}{2}\left(\frac{1}{\ell^2} - \frac{1}{\delta^2}\right) u_0^2 + \int_0^{u_0} du \, \frac{T_s}{\delta^2} \frac{\rho_0 u}{\eta_0 P} = 0, \tag{55}$$

which may be rearranged to give

$$\left(\frac{1}{\ell^2} - \frac{1}{\delta^2} + \frac{\rho_0 T_s}{\delta^2 \eta_0 P}\right) u_0^2 = 0. \tag{56}$$

Using the expression for T_s, one gets

$$\sigma_{xy} = \mu_d P, \tag{57}$$

with $\mu_d = \{\eta_0 \epsilon_0 / \rho_0 d^3 (1 - \delta^2/\ell^2)\}^{1/2}$.

Although the model we have developed is purely a hydrodynamic model, this relationship is usually referred to as *solidlike* behavior.

The temperature at the boundary may be obtained from the second condition Eq. (54). The integral on the right-hand side of Eq. (54) is dominated by the behavior near $u \simeq u_0$, with $\overline{\eta}(\rho_0 m u^2/P) \simeq P/\rho_0 m u^2$ and $V(u) \simeq V(u_0) = -u_0^2/2\ell^2$. One thus gets

$$U \simeq \frac{\sigma_{xy} d^2}{m^{1/2}} \frac{\ell}{u_0} \int_0^{u_0} du \;\; \frac{m\rho_0 u}{\eta_0 P} = \frac{\sigma_{xy}}{P} m^{1/2} \frac{\rho_0 d^2 \ell}{2\eta_0} u_0, \tag{58}$$

which gives eventually

$$T_0 = m u_0^2 = \zeta_d m U^2, \tag{59}$$

where the numerical prefactor ζ_d is defined as $\zeta_d = [2\eta_0/(\mu_d \rho_0 d^2 \ell)]^{1/2}$.

This shows that the large velocity regime that we defined as $T_0 > P/\rho_0$ ratifies $U > [P/(\mu_t m \rho_0)]^{1/2} \sim (P d^3/m)$.

(ii) Small velocity limit: In this case the viscosity is expected to behave ''anomalously,'' with $\overline{\eta}(\rho_0 m u^2/P) \simeq \eta_1 (P/\rho_0 m u^2)^\beta$. In this limit, the first condition, Eq. (50), then takes the form

$$0 = \frac{1}{2}\left(\frac{1}{\ell^2} - \frac{1}{\delta^2}\right) u_0^2 + \int_0^{u_0} \frac{du}{u} \frac{T_s}{m\eta_1 \delta^2} \left(\frac{m\rho_0 u^2}{P}\right)^\beta, \tag{60}$$

which can be reorganized to give

$$\sigma_{xy} = P \left[\left(1 - \frac{\delta^2}{\ell^2}\right) \frac{\beta \eta_1 \epsilon_0}{\rho_0 d^3}\right]^{1/2} \left(\frac{\rho_0 m u_0^2}{P}\right)^{1-\beta/2}. \tag{61}$$

This equation has to be completed by the second condition Eq. (54). In this equation, the potential term $V(u)$ may be approximated by $V(u) \simeq (1/2\delta^2) u^2$, since the temperature $T = mu^2$ is small (see the discussion of the shape of the potential in the previous subsection). Together with the asymptotic expression of the viscosity in this limit, one may rewrite Eq. (54) as

$$U = \frac{\sigma_{xy} d^2}{m\eta_1} \int_0^{u_0} \left(\frac{m\rho_0}{P}\right)^\beta u^{2\beta-1} \frac{du}{\sqrt{\frac{1}{\delta^2} u^2}}, \tag{62}$$

which yields

$$U = \left(\frac{P}{m\rho_0}\right)^{1/2} \frac{\sigma_{xy}}{P} \frac{\rho_0 d^2 \delta}{2\beta - 1} \left(\frac{\rho_0 m u_0^2}{P}\right)^{2\beta - 1/2}. \tag{63}$$

When combined with Eq. (61), one gets the following relationship between shear stress σ_{xy} and U:

$$\sigma_{xy}=\mu_W P\left\{U^2\left(\frac{m\rho_0}{P}\right)\right\}^{1-\beta/2\beta}. \quad (64)$$

The temperature at the boundary is then given as

$$T_0=\zeta_W\frac{P}{\rho_0}\left\{U^2\left(\frac{m\rho_0}{P}\right)\right\}^{1/2\beta}, \quad (65)$$

where the two numerical prefactors μ_W and ζ_W are defined as $\mu_W=[(1-\delta^2/\ell^2)(\epsilon_0/\rho_0 d^3)\beta\eta_1]^{(2\beta-1)/(2\beta)}(2\beta-1/\rho_0 d^2\delta)^{(1-\beta)/\beta}$ and $\zeta_W=[(2\beta-1)/(\mu_W\rho_0 d^2\delta)]^{1/(2\beta-1)}$. The stress crosses over from its low velocity power-law in velocity behavior to its high-velocity constant value at $U\approx U_c=P/(m\rho_0)$.

A crucial feature of the U dependence of shear stress in this regime is that it is **velocity weakening**, i.e., the shear stress decreases with increasing U for $U<U_c$ because $\beta>1$.

4. General remarks about shear forces at constant pressure

Before ending this section, we would like to emphasize a few points:

We have identified two regimes in the shearing velocity dependence of the shear force. For *small velocities*, the shear force is *velocity weakening*, as obtained in Eq. (64). For *large velocities*, the shear force is found to be ''*solidlike*,'' i.e., independent of the shearing velocity, and proportional to pressure, as shown in Eq. (57).

The cross-over between one regime and the other is found to occur at a *critical velocity*, $U_c=(Pd^3/m)^{1/2}$.

In the velocity weakening regime, i.e. for velocities smaller than U_c, the steady sliding regime is expected to be unstable. Indeed, as $\partial\sigma_{xy}/\partial U<0$, the steady sliding situation is unstable to small fluctuations (see Refs. [45,46] for a full discussion). As a result, one might expect a *stick-slip behavior of the system for* $U<U_c$. Note, however, that the present model cannot be used to describe the whole stick-slip cycle since it is expected to fail at a vanishing velocity, i.e. during the stick period. How this prediction relates to the stick-slip to steady sliding transition will require further study.

Finally, it is interesting to note that both the large and small U limits of the shear rates Eqs. (57) and (64) are in agreement with our previous dimensional analysis of the dynamics in the constant volume case (see Sec. V D 1). Since on dimensional grounds the pressure should be proportional to U^2 when the volume is fixed, one finds that both expressions reduce to the Bagnold scaling $\sigma_{xy}\propto U^2$. We emphasize that this ''global'' scaling holds even if the local Bagnold relationship $\sigma_{xy}\propto\dot{\gamma}^2$ is not expected to hold in the small velocity regime (where the viscosity exhibits an ''anomalous'' behavior).

VI. CONCLUSIONS

In this paper, we have investigated both experimentally and theoretically the shear dynamics of granular flow. The granular material was sheared in a Couette cell, instrumented to allow measurements of both shear forces and ''microscopic'' dynamics of individual particles. The latter measurements were performed by tracking the instantaneous positions of particles on the upper surface using a fast camera and an imaging procedure. A variable upward air flow through the granular material allows the internal pressure to be adjusted. Experimentally, the following results were found: (i) granular flow is restricted to a small region close to the moving boundary; (ii) the normalized velocity profile is independent of the shearing velocity, pressure (i.e., airflow), and of the type of motion of the moving cylinder (stick-slip or continuous sliding); (iii) the shear force acting on the moving cylinder is independent of the shearing velocity and proportional to pressure, as shown in the planar geometry in [36]; (iv) there is a close connection between local fluctuations and mean flow, as manifested in the apparent power-law relationship measured experimentally between these two local quantities (Fig. 10); (v) the rms velocity profile decays more slowly as a function of the radial coordinate than does the mean-velocity profile. However, we have cautioned that the functional form of the fluctuation profiles could be affected by frame rate limitations. We find that these general features occur for several different types of particles, though there are quantitative differences.

On the basis of these observations, we have proposed a ''hydrodynamic'' model for the granular flow, in which the granular material is assumed to behave similar to a locally Newtonian fluid. In contrast to ''classical'' fluids however, the temperature and density of the material are not constant over the shear cell. The temperature, defined in terms of the fluctuations of the velocity, is created at the moving boundary and propagated through the material. The temperature profile thus results from a balance between heat flux and local energy loss due to the inelasticity of collisions. As a consequence, the density and temperature dependences of the transport coefficients play a crucial role.

In the high-density regime under consideration, simple, asymptotic expressions for the transport coefficients may be obtained within the Enskog approximation. The latter is however expected to be invalid for the density dependence of the viscosity at very high densities (close to random close packing, RCP) where collective rearrangements comes into play. This led us to assume a stronger divergence of the viscosity as a function of the density close to RCP. In a manner analogous to what is usually proposed in supercooled liquids, we have assumed an algebraic divergence of the viscosity near the RCP density. Using the equations of transport of momentum and heat, we then compute the mean and rms-velocity profiles. Those are found to be in very good agreement with the experimental results. Moreover, the scaling law relationship between the mean- and rms-velocity profiles that is found experimentally is also predicted from the model; though the experimental results may be affected by frame rate limitations of our measurements.

Finally, the velocity dependence of the shear force is determined. Two regimes are predicted, depending on whether the velocity is larger or smaller than a critical velocity $U_c=(Pd^3/m)^{1/2}$. For large velocities, a *solidlike friction force* is predicted, i.e., independent of the shearing velocity, in

agreement with the experimental observation. For small velocities, a *velocity weakening* regime is predicted, consistent with the occurrence of stick-slip motion in this case. We emphasize that these results are found within the hydrodynamic model, even if no solid friction force is assumed to hold between the grains. Of course, we expect the model to fail at sufficiently small U as the static regime is approached.

In our paper, we have assumed that the flow on the upper surface is close to that within the interior of the Couette cell, as found in earlier work [3]. However, since the particles on the surface are less constrained, their fluctuations could be somewhat different from those in the interior, even when we apply a downward pressure through an airflow. While MRI and x-ray measurements in the interior [3] could not resolve fluctuations, recent measurements of fluctuations on the more constrained bottom surface layer by the Chicago group [47] reveal fluctuation profiles similar to ours: Fluctuations decay with a characteristic length longer than that for the mean velocity. As in our experiments on the top surface, fluctuations are found to be proportional to the velocity gradient to a power close to 0.5. The scaling holds over three orders of magnitude in velocity gradient in these measurements. The velocity profiles found in these two experiments differ somewhat; however, differences in geometry (inner and outer radii), material properties, and measurement methodology make a direct comparison between the experiments difficult.

The main point of the present paper is the agreement between our measured velocity profiles (in particular the confinement of velocity gradients to a thin shear band) and friction force and the predictions of a Newtonian hydrodynamic model with a strong density dependence of the viscosity taken from models of the glass transition.

Many questions are still open. One important problem, which is not discussed here, is the temporal response of the system when a velocity step is imposed. Such an experiment would provide information about the transport mechanism within the granular material. The response may be predicted in principle from the hydrodynamic model and could provide an independent test of its validity.

ACKNOWLEDGMENTS

We thank D. Howell and S. Luding for providing data to us, and M. Ernst, H. Jaeger, J. Jenkins, and S. Nagel for valuable discussions. J.P.G. acknowledges helpful discussions at the Aspen Center for Physics. This work was supported by the National Science Foundation under Grant Nos. DMR-9704301 and DMR-0072203 to Haverford College, and DMR-9730405 and DMR-9632598 to The University of Pennsylvania.

[1] E. Clement, Curr. Opin. Colloid Interface Sci. **4**, 294 (1999).
[2] R.P. Behringer *et al.*, Physica D **133**, 1 (1999).
[3] D.M. Mueth *et al.*, Nature (London) **406**, 385 (2000).
[4] W. Losert, J.-C. Geminard, S. Nasuno, and J.P. Gollub, Phys. Rev. E **61**, 4060 (2000).
[5] N. Menon and D.J. Durian, Science **275**, 1920 (1997).
[6] V.V.R. Natarajan, M. Hunt, and E.D. Taylor, J. Fluid Mech. **304**, 1 (1995).
[7] S. Warr, J.M. Huntley, and G.T.H. Jacques, Phys. Rev. E **52**, 5583 (1995).
[8] G.I. Tardos, M.I. Khan, and D.G. Schaeffer, Phys. Fluids **10**, 335 (1998).
[9] E. Aharonov and D. Sparks, Phys. Rev. E **60**, 6890 (1999).
[10] W. Losert, L. Bocquet, T.C. Lubensky, and J.P. Gollub, Phys. Rev. Lett. **85**, 1428 (2000).
[11] R.A. Bagnold, Proc. R. Soc. London, Ser. A **225**, 49 (1954); **295**, 219 (1966).
[12] J.T. Jenkins and S.B. Savage, J. Fluid Mech. **130**, 187 (1983).
[13] P.K. Haft, J. Fluid Mech. **134**, 401 (1983).
[14] C.S. Campbell, Annu. Rev. Fluid Mech. **22**, 57 (1990).
[15] S.B. Savage, in *Continuum Mechanics in Environmental Sciences and Geophysics*, edited by K. Hutter (Springer, New York, 1993).
[16] J.T. Jenkins and E. Askari, J. Fluid Mech. **223**, 497 (1991).
[17] S.B. Savage and K. Hutter, J. Fluid Mech. **199**, 177 (1989).
[18] K. Hutter, in *Continuum Mechanics in Environmental Sciences and Geophysics*, edited by K. Hutter (Springer, New York, 1993).
[19] B. Miller, C. O'Hern, and R.P. Behringer, Phys. Rev. Lett. **77**, 3110 (1996).
[20] D.M. Mueth, H.M. Jaeger, and S.R. Nagel, Phys. Rev. E **57**, 3164 (1998).
[21] R. Gutfraind and O. Pouliquen, Phys. Rev. E **53**, 552 (1996).
[22] G. Debregeas and C. Josserand, Europhys. Lett. **52**, 137 (2000).
[23] P. Mills, D. Loggia, and M. Tixier, Europhys. Lett. **45**, 733 (1999).
[24] T.S. Komatsu, S. Inagaki, N. Nakagawa, and S. Nasuno, Phys. Rev. Lett. **86**, 1757 (2001); e-print cond-mat/0008086(2000).
[25] G.D. Scott and D.M. Kilgour, Br. J. Appl. Phys., J. Phys. D **2**, 863 (1969).
[26] C. Donati *et al.*, Phys. Rev. Lett. **80**, 2338 (1998).
[27] B.J. Alder, D. Gass, and T. Wainwright, J. Chem. Phys. **53**, 3813 (1970).
[28] E. Leutheusser, J. Phys. C **15**, 2801 (1982); **15**, 2826 (1982).
[29] E.R. Weeks *et al.*, Nature (London) **287**, 627 (2000).
[30] A.J. Liu and S.R. Nagel, Nature (London) **396**, 21 (1998).
[31] We neglect air flow mediated particle-particle interactions.
[32] S. Nasuno, A. Kudrolli, and J.P. Gollub, Phys. Rev. Lett. **79**, 949 (1997).
[33] C.S. Campbell and A. Gong, J. Fluid Mech. **164**, 107 (1986).
[34] J.T. Jenkins and M.W. Richman, J. Fluid Mech. **192**, 313 (1988).
[35] I. Goldhirsch and N. Sela, Phys. Rev. E **54**, 4458 (1996).
[36] J.-C. Geminard, W. Losert, and J.P. Gollub, Phys. Rev. E **59**, 5881 (1999).
[37] S. Schöllmann, Phys. Rev. E **59**, 889 (1999).
[38] J.P. Hansen and I.R. McDonald, *Theory of Simple Liquids*, 2nd ed. (Academic Press, London, 1986).

[39] V. Garzò and J.W. Dufty, Phys. Rev. E **59**, 5895 (1999).
[40] R.J. Speedy, J. Chem. Phys. **110**, 4559 (1999).
[41] L.V. Woodcock and C.A. Angell, Phys. Rev. Lett. **47**, 1129 (1981).
[42] W. Goetze and L. Sjoegren, Rep. Prog. Phys. **55**, 241 (1992).
[43] J.-L. Barrat, W. Goetze, and A. Latz, J. Phys.: Condens. Matter **1**, 7163 (1990).
[44] D. Howell, R.P. Behringer, and C. Veje, Phys. Rev. Lett. **82**, 5241 (1999).
[45] F.J. Elmer, J. Phys. A **30**, 6057 (1997).
[46] B.J. Persson, *Sliding Friction* (Springer-Verlag, Berlin, 1998).
[47] D.M. Mueth, e-print cond-mat/0103557(2001).